Dolostone pulverization induced by coseismic rapid decompression of CO2-rich gas in nature (Matese, Apennines, Italy)

Dolostone pulverization induced by coseismic rapid decompression of CO_2-rich gas in nature (Matese, Apennines, Italy)

Andrea Billi[1*], Luca Smeraglia[1], Luca Aldega[2], Fabrizio Balsamo[3], Marino Domenico Barberio[2], Chiara Boschi[4], Antonio Caracausi[5], Eugenio Carminati[2], Alessandro Iannace[6], Marco Mercuri[2], Mattia Pizzati[3], Stefano Tavani[1,6]

[1] Consiglio Nazionale delle Ricerche, IGAG, Rome, Italy.

[2] Department of Earth Sciences, Sapienza University of Rome, Italy.

[3] Department of Chemistry, Life Sciences and Environmental Sustainability, University of Parma, Italy.

[4] Consiglio Nazionale delle Ricerche, IGG, Pisa, Italy.

[5] Istituto Nazionale di Geofisica e Vulcanologia, Palermo, Italy.

[6] Dipartimento di Scienze della Terra, dell'Ambiente e delle Risorse, University of Naples, Italy.

[*] corresponding author: Andrea Billi, Consiglio Nazionale delle Ricerche, IGAG, at Department of Earth Sciences, Sapienza University of Rome, Geochimica Building, P.le A. Moro 5, 00185, Rome, andrea.billi@cnr.it

Abstract

South Matese, Apennines, is a hydrothermally and seismically active extensional area characterized by CO_2 outgassing and Mw ≤7.1 earthquakes. There, meters-sized pockets of incohesive pulverized dolostone are hosted within Mesozoic carbonates at the hanging wall of seismically active normal faults. The aim of this paper is to understand the pulverization process. The pulverized dolostone is finely comminuted (down to a few microns), but primary structures, mainly bedding, are preserved. The grain size distribution is similar to that of previously studied pulverized rocks associated with active faults and dissimilar to that of carbonate cataclasites and fault gouges. The pulverized pockets are surrounded by zones (halos), in which the loose grains are cemented, in their original position, by microcrystalline calcite, resulting in a cemented micro-mosaic breccia. Stable isotopes from the cement are compatible with calcite precipitation from rapidly CO_2-degassing shallow waters. Comparing our observations with results of laboratory experiments on carbonate pulverization through rapid decompression of pore-hosted CO_2, the best explanation for the pulverized dolostone may lie on local accumulations of pressurized CO_2-rich gas, suddenly decompressed during earthquakes. The limited permeability of the gas-saturated dolostone must have prevented a prompt escape of the gas from the rock, which was therefore anhydrously pulverized by the rapid expansion of the trapped gas. The sudden decompression must have suctioned bicarbonate-rich groundwaters, from which microcrystalline calcite rapidly precipitated, fossilizing the freshly pulverized dolostone. Calcite precipitation formed an impermeable shield around the pulverized pockets, which, therefore, remained internally uncemented. This process may have occurred over multiple cycles at depths shallower than the CO_2 subcritical–supercritical boundary (ca. -800 m). Although hypothetical, the proposed mechanism is for the first time suggested for an active tectonic environment. This case may improve our knowledge of

possible chemical-physical processes connected with the subsurface storage of CO_2 in seismically active areas.

1. Introduction

Pulverized rocks are extremely comminuted low-strain rocks in which the micro-clasts are almost in their original position such as to resemble a micro jigsaw puzzle. Pulverized rocks are typically found in low permeability rocks, such as crystalline or tight carbonate rocks, and even when these rocks occur within fault zones (as it usually happens), they are markedly different from cataclastic rocks and fault gouges in terms of grain size distribution, texture, and position within the deformation zone (Brune, 2001; Dor et al., 2006; Rockwell et al., 2009; Muto et al., 2015; Schröckenfuchs et al., 2015; Williams et al., 2021). Due to these peculiar structural features and their occurrence within seismically active fault zones, pulverized rocks are often considered as diagnostic of coseismic high-strain-rate deformation within shallow (<3 km depth) confined rock volumes (Wilson et al., 2005; Doan and Gary, 2009; Mitchell et al., 2011; Yuan et al., 2011; Sagy and Korngreen, 2012; Rempe et al., 2013; Aben et al., 2017b; Fondriest et al., 2017; Rodríguez-Escudero et al., 2020; Ostermeijer et al., 2022).

One interesting but poorly investigated mechanism of pulverization in active tectonic environments is the one connected with fluid (gas) pressure fluctuation within rocks. To this end, Mitchell et al. (2013) experimented with explosive pulverization of rocks by imparting rapid drops in gas confining pressure for noble gas-saturated rock samples (tonalite), using a specifically designed pressure vessel to allow near-instantaneous decompression of the rock samples. The limited permeability of the tested rocks created non-draining conditions during the rapid decompression experiments, resulting in the pulverization of the samples due to the sudden expansion of the gas trapped within the rock pores, unable to drain quickly from the rock (Mitchell et al., 2013). These promising laboratory experiments - recently substantiated by further similar experiments on carbonate using CO_2 as the rapidly expanding gas (Hesse et al., 2022) - were not validated on natural examples. Hence, the pulverization mechanism via rapid decompression of gases within rocks remains experimentally operable but still elusive in nature, at least in active seismic domains.

We present a multidisciplinary study of pulverized dolostone exposed in the hanging wall of the south Matese normal fault system, Apennines, Italy (Fig. 1a). This site is ideal to study possible relationships between natural faulting, active fluid circulation, and rock pulverization in a seismically active region. The study area is indeed characterized by (1) seismically active normal faults (Boncio et al., 2022), (2) extensive exposure of dolostone, which is a rock type elsewhere documented to be often pulverized (Agosta and Aydin, 2006; Sagy and Korngreen, 2012; Schröckenfuchs et al., 2015; Fondriest et al., 2017; Kaminskaite et al., 2020), and (3) active circulation of CO_2-rich fluids (Figs. 1b and 1c) that may partially derive from the nearby active or quiescent volcanic districts (Di Luccio et al., 2018; Santo et al., 2019). Our main goal is to understand the mechanism of dolostone pulverization.

2. Pulverization Models

Although an increasing number of papers has been dedicated to this issue, no unique or broadly accepted explanations of how pulverized rocks form in nature are available (Aben et al., 2017a; Payne and Duan, 2017; Ostermeijer et al., 2022). To contextualize our results and establish the best model for the natural pulverization described in this work, we here provide a brief review of existing laboratory and numerical models for the genesis of pulverized rocks:

(1) Dynamic unloading: faulting along a bimaterial interface implies an abrupt reduction of normal stress at the fault tip. This produces a tensional wave that fractures the rock in fault-proximal domains in an event similar to a rock-burst due

to volumetric tensile expansion (Ben-Zion and Shi, 2005; Dor et al., 2006; Payne and Duan, 2017).

(2) Dynamic fragmentation: during very rapid coseismic strain rates, multiple fractures can propagate simultaneously before any appreciable stress is relieved. This process breaks the rock into fragments without shearing. Supershear faulting (when a fault rupture propagates faster than the shear wave speed) produces shock wave fronts that feature large changes in strain rate over a very small volume. As such, this mechanism is a good candidate for rock pulverization through dynamic fragmentation in fault-proximal domains (Doan and Gary, 2009; Doan and Billi, 2011; Wechsler et al., 2011; Yuan et al., 2011; Doan and d'Hour, 2012).

(3) Transient tensile pulses: pulverized rocks found even 100 m away from the principal slip zone of seismogenic rupture can form during transient tensile stress perturbations created during the passage of earthquake ruptures. These ruptures and related stress perturbations are especially prevalent along bimaterial interfaces with a larger propensity to pulverization of stiffer and stronger rocks (Xu and Ben-Zion, 2017; Griffith et al., 2018; Smith and Griffith, 2022a).

(4) Rapid gas decompression: Mitchell et al. (2013) recorded an explosive pulverization mechanism within a laboratory setting by creating rapid drops in gas-confining pressure for gas-saturated (effectively unconfined) crystalline rock samples. Using a specifically designed pressure vessel that allows the instantaneous decompression of rock samples via a blow-out diaphragm, only low-permeability (10^{-19}-10^{-20} m^2) crystalline rocks were pulverized. This occurred through a sudden volumetric expansion driven by pore fluid where the confining pressure dropped faster than the pore pressure of the rock. The pulverized samples were characterized by non-systematically oriented pervasive

microfractures that bonded particles with size distribution from about 1 mm down to <0.01 mm. Recently, similar tests were performed by Hesse et al. (2022), who used commercial carbonate as the host rock and CO_2 as the pore-hosted gas. In a laboratory apparatus, the rock was permeated by CO_2 and both temperature and pressure were raised to supercritical CO_2 conditions. The rapid release of CO_2 into a decompression chamber resulted in an expansion of supercritical CO_2 inside the pores and consequent rock pulverization from tension. After three cycles of compression and rapid decompression, the carbonate samples were comminuted from 13.2 mm down to <300 μm particles.

In addition to the aforementioned models, coseismic processes predisposing rock to pulverization include the rapidly oscillating stresses during a single rupture potentially reducing the rock compressive strength (Braunagel and Griffith, 2019) or the occurrence of successive seismic high-strain rate loadings eventually leading to a reduction of the pulverization threshold (Aben et al., 2016).

3. Geological Setting

The studied exposure (Figs. 1–3) is located in the central-southern Apennines, a Late Oligocene to Present fold-thrust belt developed during the subduction of the Adriatic plate below the European one. Since the Early Pliocene, the internal (western) and axial parts of the central-southern Apennines belt have undergone post-orogenic exhumation and extensional faulting (Malinverno and Ryan, 1986). This extensional regime is still active and has generated a peri-Tyrrhenian volcanic system and a set of main NW-SE oriented extensional faults that are the source of Mw ≤7.1 historical and instrumental seismicity in the study area (Galli and Naso, 2009; Boncio et al., 2022) as well as the main pathway of active degassing (Ascione et al., 2018). We focused our study on the Ailano area, which is located at the south-western foot of the Matese Mts., on the hanging wall of the south Matese active normal fault system, nearby active or quiescent volcanic-hydrothermal districts (Fig. 1). In this area, the exposed stratigraphic sequence is characterized by Upper Triassic carbonate platform dolostone, upward followed by Lower Jurassic to Upper Cretaceous carbonate platform limestone and dolostone, and by syn-orogenic siliciclastic deposits (Fig. 1a). Based on the minimum thickness of the sedimentary pile previously overlying the study outcrop, we infer that the investigated area has been exhumed from a minimum depth of about 3.5 km. Obviously, this depth does not necessarily represent the depth of dolostone pulverization.

In the study area, the main fault system is extensional, NW-striking, SW-dipping, and it occurs toward the NE. The investigated area is therefore located on a wide and fractured-faulted hanging wall block (Fig. 1a). The subsurface structural architecture of this hanging wall block is substantially unknown. Due to the presence of numerous active normal faults and associated degassing vents in the study area, we hypothesize, however, the presence of a set of fluid-conductive active normal fault zones beneath and in the vicinity of the studied exposure (see the cross-section in Fig. 1a), where outcrop-scale faults are directly observed (Fig. 2a).

In the study area, CO_2- and CH_4-rich (up to 30.000 g x d^{-1} and 2000 g x d^{-1} respectively; Ascione et al., 2018) gas vents and large diffusive gas emissions from soil occur close to the villages of Ciorlano and Ailano (Fig. 1), with mantle-derived fluids (e.g., CO_2, helium) that are involved in the local seismicity (e.g., Caracausi and Paternoster, 2015; Di Luccio et al., 2018). The helium isotopic signature is between 0.7 and 1 Ra (Fig. 1c, Table S1; Caracausi and Paternoster, 2015; Ascione et al., 2018; unpublished INGV data), larger than typical crustal fluid values (0.01–0.03 Ra) from cratons and sedimentary basins far from active tectonic regions (Fig. 1c). Fig. 1(c) clearly indicates that He in the Ailano-Ciorlano gases results from a mixing of mantle and crustal components, where the high flux of volatiles at the surface has been hypothesized as being driven by the presence of magmatic melts at depth beneath the Matese region (Italiano et al., 2000; Di Luccio et al., 2018).

4. Methods

We collected data and rock samples (Table S2) along a ~200 m long road cut, where fractured Lower Jurassic platform carbonates and discrete zones/pockets of pulverized carbonates are exposed (Figs. 2 and 3; Lat. 41.397729°, Long. 14.171114°). We combined the following analytical techniques on both the pulverized and the host rocks: outcrop-scale geological and structural observations and analyses; thin section analysis under optical microscope and associated cathodoluminescence, and under scanning electronic microscope (SEM) and associated Energy Dispersive Spectrometry (EDS); grain size distribution analyses: 2D image analysis and 3D laser diffraction granulometry on cohesive/impregnated and incohesive samples, respectively; X-ray diffraction analyses; geochemical analyses of major and minor elements and rare earth elements (REE); and carbon and oxygen stable isotope analyses. All methods are described in detail in the Supplemental Material.

5. Results

5.1 Field Observations

Along the studied exposure, we recognized two main types of rocks relevant to our research (Figs. 2, 3, and S1-S5): (1) cohesive host carbonates (mainly dolostone) displaying bedding and (2) pockets of incohesive pulverized carbonates (mainly dolostone) hosted within the bedded carbonates. We differentiate distal and proximal cohesive host rocks based on the distance from the incohesive pulverized pockets (distal: >10 m; proximal: <20 cm). An angular unconformity marked by overlying Quaternary breccias truncates the upper part of the exposure, made of pulverized dolostone and bedded carbonates (Fig. 2b).

The host rock consists of decimeters-thick beds of dolostone and dolomitic limestone as well as rarer limestone that are fractured and faulted (Fig. 2a). The beds are NE-dipping by about 45°. Fractures are very frequent (fracture spacing is often about 1 cm or less) and hardly systematic, although main sets include fractures striking NW–SE and dipping toward either NE or SW by about 70° or more. Faults (only 17 along the study exposure) are less frequent than joints and with very limited displacement (less than a few centimeters). Fault surfaces strike preferentially NW–SE, with a dip angle of about 60°, either toward NE or toward SW. A set of faults, N–S striking and dipping toward E by about 70°, is also present (Fig. 2a; Table S3).

The incohesive pulverized pockets are meters-sized and characterized by irregular or chimney/domal morphologies. Pulverized dolostone is usually white in color, totally incohesive, very fine-grained, and shows jagged or transitional to sharp boundaries with the fractured host rock (Figs. 2 and 3; Videos S1-S4; Virtual Outcrops S1-S4). In many cases, primary bedding is still visible within the pulverized pockets (Figs. 2b-2d and 3a; Video S4). Pebble-shaped fragments of the host rock are occasionally found within the fine-grained matrix of the pulverized dolostone (Fig. 3b). The domal pockets of pulverized dolostone appear, in some cases, upwardly bounded by a thin (2–5 cm) layer of shale or clayey marl occurring along the bedded host dolostone. At least in one case, the shale layer has an antiformal geometry around the upper portion of a domal pocket of pulverized rocks (Fig. 3e).

5.2 Microscopic Observations

The distal and proximal host rocks are characterized by a large variety of depositional/diagenetic microstructures, which are usually well preserved (Fig. 4). In the distal host rock (Fig. 4a-c), primary depositional features are perfectly preserved together with intergranular early phreatic cements and late diagenetic blocky calcite (Fig. 4a). Fine-grained crystalline dolomites display an excellent preservation of the grainstone depositional texture (Fig. 4b). In places, incomplete replacement of limestone by dolomite is recorded (Fig. 4b). A zoned and coarse crystalline dolomite within fractures and cavities and poikilotopic calcite occur (Fig. 4c), probably representing hydrothermal dolomitization. These depositional and diagenetic features are typical of Upper Triassic-Lower Jurassic shallow water carbonates from the central Apennine carbonate platform (Iannace et al., 2011).

Under optical microscope, the proximal host rock surrounding and embedding the pulverized carbonates is characterized by alternating dark and light concentric bands (Figs. 4d and 4e) consisting of a mosaic of fine-grained dolomite crystals showing equal grain sizes (Figs. 4e and 4f). The former sedimentary structures are perfectly decipherable within the banded zones (Figs. 4c and 4d). The fine-grained dolostone crystals are non-luminescent (Figs. 4g, 4h, and S4a–S4f) and, in places, are cut by <1 mm thick microfractures filled by blocky calcite crystals showing a dull red and zoned luminescence color (Figs. 4g and 4h).

SEM observations, together with EDS analyses, revealed that dolomite (of both distal and proximal host rocks) consists of fine-grained crystals (Figs. 5a–5c, S1, and S2). In places, dolomite crystal boundaries are visible (Figs. 5a, 5b, and S1), while in other cases, crystals are well welded (Figs. 5c and S1). Intergranular porosity occurs between the crystals (Figs. 5a–5c, S1e-S1h, and S3a). Occasionally, calcite-filled veins crosscut the fine-grained dolomite crystals (Figs. 5a and S2c–S2e).

SEM observations further reveal the micro-texture of the proximal cohesive host rock, which consists of grains immersed in a microcrystalline calcite cement, each grain being formed by single crystals or more often by aggregates of dolomite crystals. The resulting pattern is a cemented micro mosaic or crackle-like breccia (Fig. 5e-5i, S2c-S2h, S3b, S3c, and S5b). The microcrystalline calcite cement displays a dominant black color under cathodoluminescence, with rare bright orange rims along the outer crystal edges (Fig. S4e and S4f). No substantial shear displacement is observed along the microfractures (i.e. between the grains), which are non-systematically oriented and mostly coincide with the crystal (or crystal–aggregate) boundaries. The dolomite crystals contain widespread micropores (Figs. 5e, 5f, S1f–S1h, S3a, and S3b). Crystal boundaries are generally sharp; however, in places, these boundaries may be rounded or with embayment-like morphologies (Figs. 5e, 5f, S2c, and S2d). The transition toward bands dominated by microcrystalline calcite cement is diffuse and is characterized by dolomite crystals fading within the calcite cement (Figs. 5f and S2d). Small, rounded pockets of fine grained (pulverized) dolomite grains also occur (Figs. 5h, 5i, and S2e-S2g). In these pockets, no calcite cement is present while, in contrast, calcite cement is present all around them. Occasionally, <100 μm thick calcite filled veins cut across the dolomite crystals (Figs. 5g, 5i, and S2g).

At the micro-scale, pulverized incohesive carbonates sampled within the pulverized pockets consist of dolostone grains with sharp boundaries (Figs. 5k, 5l, S2h, and S3d). The rhombohedral habit of dolostone crystals is still preserved, although the crystal faces are often characterized by small cavities (Figs. 5k-l and S3d). The dolostone grains consist of single crystals or, in places, crystal aggregates (Fig. 5k). As a synthesis of our micro-observations, Fig. S5 shows a micro-comparison between incohesive pulverized dolostone and cohesive distal and proximal host rocks.

5.3 Grain Size Distributions

The incohesive pulverized dolostone (dolostone grains from pulverized pockets; Figs. 5k and 5l) were analyzed both through the 3D method (laser granulometry) and through the 2D image analysis method (on SEM photomicrographs using epoxy-impregnated samples; e.g. Fig. 5k) whereas the cohesive host rocks (dolostone in Figs. 5a-5c and cemented mosaic breccias in Figs. 5d–5f) only through the 2D method. All grain size distributions are unimodal and well sorted. Results are as follows (Fig. 6).

Distal host rocks: grain sizes are between 2 and 90 μm in diameter (coinciding with the size of dolomite crystals); mean grain diameters are between 10.5 and 47.8 μm, with modal values of distribution curves between 5.2 and 11.2 μm (Fig. 6a)

Proximal host rocks (mosaic microbreccias): the grain size distributions are comprised between 4 and 200 μm in diameter (coinciding mainly with the size of dolomite crystals and to a lesser extent with the size of crystal aggregates); mean grain diameters are between 66.3 and 86.1 μm with modal values of distribution curves falling between 18.7 and 31.1 μm (Fig. 6b). The shift towards coarser grain size fraction can be related to the presence of polycrystalline aggregates.

Pulverized dolostone (2D image analysis): grain size distribution curves are comprised between 8 and 1100 μm in diameter; mean grain diameters are between 247.4 and 786.8 μm, with modal values of distribution curves between 18.7 and 41.1 μm (Fig. 6c). Higher values of average diameters are due to the occurrence of mm-size crystal aggregates (e.g. Fig. 5k).

Pulverized dolostone (3D laser granulometry analysis): grain size distributions fall between 1 and ~2000 μm in diameter; mean grain diameters are between 57.8 and 153 μm, with modal values of distribution curves between 42.9 and 106 μm (Fig. 6d).

SEM observations on the incohesive or impregnated pulverized dolostone show that the grains are made up of individual dolomite crystals of 20–30 μm in size or by dolomite crystal aggregates spanning from 70–90 μm up to 1500 μm (Figs. 5k, 5l, S3d, and S20-22). All results from grain size analyses are summarized in Tables S4 and S5 and in Figs. S6–S22.

5.4 Bulk X-Ray Diffraction

We performed X-ray semiquantitative analyses of the bulk composition of eleven samples from the cohesive host rock (proximal and distal), ten samples from the incohesive pulverized dolostone, and three samples from the shale or clayey marl occurring along the bedded host rock (Fig. 7 and Table S6). The distal host carbonates include two endmembers: the first one is characterized by prevailing dolomite (between 91 and 93%) and low calcite contents (7–9%), and the second one is entirely composed of calcite (99%) with very low dolomite content, not exceeding 1% (Fig. 7). Samples from the proximal host rock show variable amounts of dolomite, in the range of 63 to 98% (average 81%), and calcite, between 2 and 37% (average 19%; Fig. 7). The pulverized rocks show greater amounts of dolomite (from 85 to 100%, average 98%) and smaller amounts of calcite (from 0 to 10%, average 2%; Fig. 7) than their counterparts in the host rock. Occasionally, sheet silicates occur in the pulverized rocks, with contents lower than 6% (Fig. 7). In a few pulverized samples, traces of norsethite $BaMg(CO_3)_2$, a mineral belonging to the dolomite group, occur. Shale interbedded with dolostone layers contain sheet silicates (mica, chlorite, and kaolinite) with amounts ranging between 70 and 89%, calcite (6–24%), hematite (2–4%), and minor amounts of quartz (1–2%) and dolomite (1–2%) (Fig. 7). Traces of gypsum were observed in the X-ray tracings (Supplemental Diffractograms).

5.5 Bulk and Punctual Analyses of Stable Isotopes

Stable isotope analyses show that both proximal and distal host rocks and pulverized dolostone are characterized by similar values of δ^{13}C and δ^{18}O (Fig. 8a and Table S7). We acknowledge that these results refer to bulk analysis (i.e., without separating dolomite and calcite components in the samples). In particular, δ^{13}C values show a narrow range, between +2.5 ‰ and +4.0 ‰ V-PDB, whereas δ^{18}O values range between +28.0 ‰ and +33.0 ‰ V-SMOW (Fig. 8a). Such values are typical for most marine carbonates, particularly the Jurassic-Cretaceous ones in the central Apennines (e.g., Agosta and Kirschner, 2003).

We also performed punctual stable isotope analyses on a set of micro subsamples that were collected along four centimeter-scale transects across banded calcite with dolomite grains in cohesive proximal host rocks (see the analyzed samples in Fig. S23). Similar banded calcite is visible nearby cemented mosaic breccias also in Figs. 5d, 5f, and S2d. The $\delta^{18}O_{calcite}$ values show a narrow range, between +26.0 ‰ and +28.0 ‰, whereas the $\delta^{13}C_{calcite}$ values show a wide range, between +3.0 ‰ and +8.0 ‰ (see calcite transects in Figs. 8a and 8b). The $\delta^{18}O_{dolomite}$ values show a range between +31.0 ‰ and +37.0 ‰, whereas, similarly to $\delta^{13}C_{calcite}$, the $\delta^{13}C_{dolomite}$ values show a wider range, between +3.0 ‰ and +8.0 ‰ (see dolomite transects in in Figs. 8a).

5.6 Bulk Analysis of REE and Minor Chemical Elements

Bulk analyses (i.e., without separating dolomite and calcite components in the samples) of REE (rare Earth elements) and minor chemical elements from (distal and proximal) host rocks and pulverized dolostone show similar patterns (Figs. 8c and 8d, Table S8). In particular, minor element concentration spans from 0.01 ppm to 1,000 ppm. The abundance of REE in pulverized dolostone and host rocks shows large variations, ranging from 0.002 ppm to 0.025 ppm. No anomalous concentrations were observed (Figs. 8c and 8d).

The PAAS-normalized (Post-Archean Australian Shales) patterns show that the REE concentrations in the host rock and in the pulverized dolostone are in the range that is typical for the Mesozoic carbonates in the central Apennines (Fig. 8d; Castorina et al. 2020). Most samples show a negative Ce anomaly (Fig. 8d), typical of marine carbonates, and La/Sm and La/Yb ratios <1 (Fig. 8d), typical of carbonate rocks in late diagenetic conditions (Fig. 8d).

6. Discussion

6.1 Pulverized Rocks

The first issue to be discussed is whether the studied rocks are truly pulverized rocks (*sensu* Brune, 2001 and Dor et al., 2006) or otherwise cataclasites or fault gouges. The following features suggest a pulverized nature of the studied rocks: (1) the very fine grained and unimodal size distribution of clasts is similar to those of previously studied pulverized rocks (Muto et al., 2015; Schröckenfuchs et al., 2015; Williams et al., 2021; Hesse et al., 2022) and dissimilar to those of polymodal and poorly sorted cataclastic rocks and fault gouges (Reches and Dewers, 2005; Cortinovis et al., 2019; Fig. 9); (2) the distribution in discrete pockets (Fig. 2) is very different from the typical occurrence of fault-parallel and proximal (often tabular) bands of cataclastic rocks and fault gouges (e.g. Reches and Dewers, 2005; Williams et al., 2021); and (3) the preservation of primary structures, such as bedding, within the pulverized pockets (Figs. 2b-2d and 3a) is typical of all pulverized rocks so far studied (e.g. Ostermeijer et al., 2022, and references therein). Indeed, these latter structures, together with the cemented micro-mosaic breccias (Figs. 5d–5f) surrounding the incohesive pulverized rocks, show that the pulverized dolostone was essentially shattered in situ without significant clast rotations, translations, and shear, as documented for many previously studied pulverized rocks (Dor et al., 2006; Ostermeijer et al., 2022). Moreover, pulverized rocks, both from dolostone (Fondriest et al., 2017) and from crystalline rocks (Rempe et al., 2013; Rodríguez-Escudero et al., 2020), are usually characterized by non-systematically oriented micro-fractures separating the single grains. A non-systematic pattern of fractures separating the single grains is also visible in the micro-mosaic breccias studied in this work (Figs. 5e and 5f).

6.2 Pulverization and Cementation

To understand the pulverization process, we start from some main observations. The pulverized dolostone is entirely incohesive and surrounded by a rock halo, i.e. the proximal host rock, which consists of cemented micro-mosaic breccias. The perfect preservation of details of the sedimentary features clearly indicates that the rocks suffered intense microfracturing with minimal strain. Moreover, the perfect polygonal fitting of dolomite clasts indicates that they are almost in their original position (Figs. 5d–5f) and the related grain size distribution is very similar to that of the incohesive pulverized dolostones apart from a few coarse-grained aggregates (Fig. 5k; compare the modal peaks of Figs. 6b-6d). Hence, it seems reasonable to infer that the pulverization process was predominantly anhydrous and was soon after followed by arrival of mineralizing fluids with rapid calcite cementation in the proximal zones, fossilizing the pulverized grain pattern and forming a low permeability cohesive shield (halo) around the incohesive pulverized dolostone. The banded pattern, in places, of the calcite cement (Fig. S23) may indicate successive cycles of cement growth, but we cannot determine the rate (rapid vs. slow) of successive band development. Repeated cycles of pulverization and post-pulverization cementation may have also occurred, but we have no clear clues to identify them.

The host rock is very heterogeneous, with varying amounts of calcite and dolomite constituting the two endmembers (Fig. 7). Therefore, we cannot infer whether the pulverization process chemically altered one of the endmembers (calcite and dolomite); however, the incohesive pulverized pockets are almost entirely made up of dolomite (average content = 98%; Fig. 7). This evidence suggests that pulverization affected almost pure dolostone, as previously observed elsewhere in faulted carbonates (Fondriest et al., 2017). Since, in fact, the pulverization process often operates by breaking apart the crystal boundaries (inter- rather than intra-crystalline fractures; Doan and Billi, 2011), the microcrystalline texture of (sedimentary) limestone can prevent the pulverization itself (e.g. dilation breccias in limestone; Tarasewicz et al., 2005) due to an excessive energy necessary to break apart every microcrystalline boundary, whereas the macrocrystalline pattern of many dolostones is more prone to pulverization (Fondriest et al., 2017; Kaminskaite et al., 2020). The same applies to the macrocrystalline (Carrara) marble (Doan and Billi, 2011).

In the same way as the X-ray diffraction, also bulk geochemical analyses (i.e., where the calcite cement was not separated by the host rock) do not allow us to identify sharp differences in minor elements or REE between the analyzed rocks (Fig. 8c and 8d). Yet, the punctual isotope analyses on the calcite cement show a different pattern with respect to the rest of the analyzed samples (Figs. 8a and 8b). In particular, the reduced values of $\delta^{18}O$

(around 27 ‰ instead of 30 ‰ V-SMOW) and the increasing values of $\delta^{13}C$ (from 3 ‰ to almost 8 ‰ V-PDB) for the calcite cement analyzed in samples A1.1, A1.1bis, A1.3, and A4.2 (Figs. 8a, 8b, and S23) are compatible with a trend of isotope fractionation of carbon dissolved in water during calcite cement precipitation from a parent solution that rapidly degassed CO_2 (Baldermann et al., 2020). Di Luccio et al. (2018) found similar carbon isotope values (from 3 to 8 ‰ V-PDB) in active springs in the Matese area and ascribed this pattern to CO_2-degassed waters possibly containing a deep CO_2 contribution. Fig. 8(a) shows that, similarly to calcite, also the dolomite contained in samples A1.1bis, A1.3, and A4.2 is characterized by an interval of $\delta^{13}C$ values from 3 to almost 8 ‰ V-PDB. This pattern may indicate an isotopic re-equilibration of dolomite grains pervaded by the above-mentioned water solution that rapidly degassed CO_2, precipitating the calcite cement.

6.3 Hypotheses and Implications

As explained in Section 2, it is not yet known how pulverized rocks form naturally (Aben et al., 2017a; Payne and Duan, 2017; Ostermeijer et al., 2022) and, consequently, any correlation between natural pulverized rocks and potential genetic models is rather speculative, including ours as follows. In particular, considering the main genetic models explained in Section 2, we believe that the first three (dynamic unloading, dynamic fragmentation, and rapidly oscillating stresses during a single rupture) could be excluded for the pulverized dolostone studied in this paper as these models are used to explain large masses of fault-proximal pulverized rocks often occurring along bimaterial interfaces. On the contrary, the pulverized dolostone studied in this paper occurs in meters-sized discrete pockets far away from major fault surfaces. Consequently, the best guess we can make relates to the rapid gas decompression model (see Section 2), which would explain why the pulverized dolostone occurs in meters-sized discrete pockets rather than in larger amasses adjacent to faults.

The above-mentioned structural and geochemical evidence, particularly the fact that the studied pulverized pockets are completely incohesive and surrounded by a halo of cemented micro-mosaic breccias, suggests us that the process of pulverization must have been somehow driven mainly by gases and related pressure fluctuations. In fact, if the system would have been dominated by CO_2-rich groundwaters, we would probably also have had calcite pervasive precipitation within the pulverized pockets. We therefore hypothesize that the dolostone pulverization was mainly driven by gas pocket accumulations and related pressure fluctuations within restricted volumes of rocks prone to be pulverized for their internal structure (see rapid gas decompression in Section 2). This hypothesis is supported by the large output of deeply-sourced CO_2-rich gases in the study area (Italiano et al., 2000; Caracausi and Paternoster, 2015; Di Luccio et al., 2018; Ascione et al., 2019). Moreover, the frequent occurrence of clay-rich layers at the top of the pulverized pockets (Fig. 3e) suggests that the gas may have accumulated in what are now the pulverized pockets, in part due to the sealing effect exerted by the clay-rich layers.

Thus, the aforementioned pulverization process by rapid decompression of the gas trapped in the rock (Mitchell et al., 2013; Hesse et al., 2022) becomes a valid candidate to explain the formation of the studied rocks. Such a process would involve a rapid expansion of a pore-trapped gas (unable to quickly drain out of the rock) due to a rapid decompression and consequent micro-fragmentation of the host rock (pulverization). We believe that the sudden gas decompression may have been triggered by one of the discussed coseismic models or processes predisposing rock to pulverization (see Section 2). For instance, we suppose the transient tensile pulses that may occur 100 m or even further away from the principal slip zone of seismogenic rupture (e.g., Bhat et al., 2012; Xu and Ben-Zion, 2017;

Griffith et al., 2018; Smith and Griffith, 2022b); however, we have no reliable clues as to what mechanism could have caused the sudden decompression.

The following evidence further supports the hypothesis of a pulverization driven by gas pressure changes. The dolomitic host rock has a primary intergranular microporosity (Figs. 5a–5c). This microporosity may have generated the appropriate level of permeability suitable to host the gas inside (through a slow saturation) but sufficiently low to prevent its escape during rapid decompression events. Mitchell et al. (2013) demonstrated that pulverization through rapid decompression of gas-saturated rocks can occur solely when intermediate-low permeability values allow sufficient rock saturation by the gas but hinder any rapid escape of the gas itself. Moreover, our micro-observations and grain size distribution analyses demonstrated that the pulverization process occurred mainly because of inter- rather than intra-crystalline fracturing (Figs. 5e and 5f). Intergranular porosity may have been decisive in localizing fractures between single crystals (interfaces between adjacent crystals) or crystal aggregates. We infer that the energy that suddenly involved the studied rocks (rapid gas expansion) was not sufficient to further break the rocks themselves and tear apart every single crystal from its neighbors or even fragment the single crystals with intra-crystalline fractures. Note also that the resulting mean grain size of the pulverized dolostone is compatible with the mean size range of previously studied fault-related pulverized rocks (e.g., Schrockenfuchs et al., 2015; Williams et al., 2021), including the fine-grained material obtained after three cycles of CO_2 decompression by Hesse et al. (2022) (Fig. 9). In Fig. 9, note that the grain size data by Hesse et al. (2022) have a lower boundary around 100 μm connected with the method of analysis (i.e., sieving).

The $CaCO_3$-cements that fossilized the micro-mosaic breccias around the pulverized pockets is microcrystalline and equigranular, and such a breccia is known to develop impulsively (Melosh et al., 2014). Hence, a reasonable hypothesis is that this cement too formed impulsively soon after the pulverization. An explanation may be that rapidly decompressed and pulverized pockets suctioned, due to the difference in pressure, nearby bicarbonate-rich waters from which microcrystalline calcite rapidly precipitated in the decompressed and pulverized pockets, consistently with the Sibson's suction pump model (Sibson, 1987, Smeraglia et al., 2016, and Brantut, 2020). The isotope data discussed above (Figs. 8a and 8b) support the precipitation of the calcite cement from a CO_2-degassed groundwater. Such a precipitation would have quickly formed a low permeability halo or shield around the incohesive pockets, which would therefore have remained protected from further mineralizing fluids. These sealing halos formed not only at the outcrop-scale but also at the micro-scale (Figs. 5h and 5i). The same type of sealing halo was also found in coseismic micro-scale pulverized and cemented carbonates along the Mt. Morrone fault (see figure S2d in Coppola et al., 2021). A shielding role (i.e. protecting the pulverized rocks from mineralizing fluids) may have been played also by the outward expansion of pressurized CO_2 right after its sudden decompression.

The model of pulverization by rapid decompression of gas-saturated rocks proposed by Mitchell et al. (2013) and Hesse et al. (2022) implies a disruptive event necessary to suddenly lower the pore pressure in the rock. We hypothesize that this type of disruptive event may have been an earthquake. The study area is highly seismic (Boncio et al., 2022) and the relationship between rock pulverization and high-energy earthquakes has been previously proposed (Ostermeijer et al., 2022, and references therein). Using the words by Rowe and Griffith (2015): "At high strain rates, the transition from discrete fracture to pulverization is governed by the rate sensitivity of fracture toughness, adding evidence that rock pulverization is a true signature of high strain rate deformation that can only be achieved during earthquake rupture or extraterrestrial impacts (Bhat et al., 2012)." However, in our study case, a cause–effect relationship between earthquakes and dolostone pulverization is speculative and should be further investigated and validated. At present, no more plausible causes than an earthquake can be proposed for the sudden decompression of the studied rocks. To this end, as mentioned above, it is noteworthy that some structures observed around the pulverized pockets were also observed in coseismic microlayers along the Mt. Morrone fault in the central Apennines (compare Figs. 5h and 5i in this work with figure S2d in Coppola et al., 2021). More in general, microcrystalline calcite precipitation along faults in different tectonic regimes can be one immediate effects of earthquake-related stress drop (e.g. Bouiller et al., 2004; Smeraglia et al., 2018). However, we cannot exclude that the rapid decompression was generated by the sudden breaking of a permeability barrier due to the accumulation of pressurized fluids itself or to the energy radiated by a nearby volcanic eruption.

6.4 Possible model

Fig. 10 synthesizes our hypothetical view of the studied pulverization process:

(1) During interseismic phases, CO_2-rich gases accumulated at the top of a bicarbonate-rich aquifer in meters-sized pockets of dolostone that is characterized by primary intergranular porosity. The gas was provided by deep sources (crust and mantle) at local and regional scale (e.g. Caracausi and Paternoster, 2015; Di Luccio et al., 2018).

(2) During disruptive events - likely high-energy seismic events - the gas underwent rapid decompression. Where the permeability was sufficiently low to prevent a prompt escape of the gas from the rock, the sudden expansion of the trapped gas within the rock pores pulverized the rock itself.

(3) Shortly after the pulverization, the decompression as well as and the permeability increase enhanced by the failure of intercrystalline boundaries suctioned the

nearby bicarbonate-saturated waters toward the pulverized pockets, where rapid cementation of the pulverized rock occurred due to microcrystalline calcite precipitation (Sibson, 1987). The rapid cementation formed a low permeability halo around the inner portion of the pulverized dolostone, which therefore remained substantially uncemented, at least in the most internal portion.

6.5 Hypothetical depth and time of pulverization

Although we have no certain constraints to adequately infer the depth of pulverization, tectono-stratigraphic data suggest that the outcrop studied should not have undergone a burial depth deeper than a few kilometers (~3.5 km). Similar to what was previously suggested for pulverized rocks exposed elsewhere, we believe that pulverization occurred at shallower burial conditions (Yuan et al., 2011). If our hypothesis of pulverization driven by rapid decompression of CO_2-rich gases is viable, then this process should have preferentially occurred above the boundary between the subcritical gaseous CO_2 (above) and the supercritical CO_2 (midway between a gas and a liquid; below) identified by many studies at approximately 800 m depth (van der Meer et al., 2009). The rapid decompression model implies indeed a rapid expansion that is a property of gases and not liquids. Considering this depth limit (800 m), we can further speculate on the age of the pulverization process by considering the average exhumation rate of 0.5 mm/yr that seems valid for most parts of the Apennines (Erlanger et al., 2022 and references therein). By multiplying this rate with the hypothetical maximum depth of 800 m for the pulverization process, we obtain a hypothetical maximum age of 400 ka for the pulverized rocks. This age matches the period of main eruptive activities in the nearby Roccamonfina Volcano (between 439 ± 9 and 148 ± 9 ka; Rouchon et al., 2008), which may have been the main source of CO_2 in the studied area, thus strengthening our hypothesis of dolostone pulverization linked with gas venting and rapid decompression in the shallow crust.

7. Conclusions

Evidence from the southwestern margin of the Matese Mts. allows us to hypothesize a new mechanism for dolostone natural pulverization, which has never been proposed in natural active tectonic environments. This mechanism implies gas (CO_2) saturation of rock during the interseismic phase and coseismic rapid decompression that makes the gas rapidly expand within the rock, thus pulverizing the host rock in situ. As shown by previous laboratory experiments, this mechanism can only work when there are appropriate intervals of permeability that hinder the rapid escape of the gas from the rock. We believe that this mechanism should be further explored, documented, and validated elsewhere before being considered as a viable process of (coseismic) deformation in active tectonic environments. It is, however, a process to consider when operating subsurface CO_2 storage. A rapid decompression of the stored CO_2 may indeed dramatically shatter the host rock, change its physical properties, and even promote the CO_2 escape outside the reservoir.

Acknowledgements

We acknowledge no funding for this study except the ordinary institutional ones (i.e. from authors' institutions; e.g. Fondi di Ateneo 2021 to E. Carminati). We thank A. Webb and an anonymous reviewer for their useful suggestions. A. Billi thanks T. Mitchell for sharing his original idea of pulverization through the rapid gas decompression. We kindly thank B. Klein and M. Hesse for providing the grain size distribution raw data of their experimentally pulverized rocks.

References

Aben, F.M., Doan, M.-L., Mitchell, T.M., Toussaint, R., Reschla, T., Fondriest, M., Gratier, J.-P., Renard, F., 2016. Dynamic fracturing by successive coseismic loadings leads to pulverization in active fault zones. Journal of Geophysical Research, 121, 2338–23360

Aben, F.M., Doan, M.-L., Gratier, J.-P., Renard, F., 2017a. Coseismic damage generation and pulverization in fault zones: Insights from dynamic Split-Hopkinson Pressure Bar experiments. In: Fault zone dynamic processes: evolution of fault properties during seismic rupture, edited by: Thomas, M. Y., Mitchell, T. M., and Bhat, H. S., Geophysical Monograph, John Wiley & Sons, Inc.

Aben, F.M., Doan, M.-L., Gratier, J.-P., Renard, F., 2017b. High strain rate deformation of porous sandstone and the asymmetry of earthquake damage in shallow fault zones. Earth and Planetary Science Letters, 463, 81–91.

Agosta, F., Kirschner, D.L., 2003. Fluid conduits in carbonate-hosted seismogenic normal faults of central Italy. Journal of Geophysical Research, 108, 2221, doi:10.1029/2002JB002013.

Agosta, F., Aydin, A., 2006. Architecture and deformation mechanism of a basin bounding normal fault in Mesozoic platform carbonates, Central Italy. Journal of Structural Geology, 28, 1445-1467.

Ascione, A., Ciotoli, G., Bigi, S., Buscher, J., Mazzoli, S., Ruggiero, L., Sciarra, A., Tartarello, M.C., Valente, E., 2018. Assessing mantle versus crustal sources for non-volcanic degassing along fault zones in the actively extending southern Apennines mountain belt (Italy). Geological Society of America Bulletin,130, 1697–1722.

Baldermann, A., Mittermayr, F., Bernasconi, S.M., Dietzel, M., Grengg, C., Hippler, D., Kluge, T., Leis, A., Lin, K., Wang, X., Zünterl, A., Boch, R., 2020. Fracture dolomite as an archive of continental palaeo-environmental conditions. Communications Earth & Environment, 1, 35, https://doi.org/10.1038/s43247-020-00040-3

Ben-Zion, Y., Shi, Z., 2005. Dynamic rupture on a material interface with spontaneous generation of plastic strain in the bulk. Earth and Planetary Science Letters, 236, 486-496.

Bhat, H.S., Rosakis, A.J., Sammis, C.G., 2012. A micromechanics based constitutive model for brittle failure at high strain rates. Journal of Applied Mechanics, 79, 031016,

Boncio, P., Auciello, E., Amato, V., Aucelli, P., Petrosino, P., Tangari, A.C., Jicha, B., 2022. Late Quaternary faulting in the southern Matese (Italy): implications for earthquake potential and slip rate variability in the southern Apennines. Solid Earth, 13, 553–582.

Boullier, A.M., Fujimoto, K., Ohtani, T., Roman-Ross, G., Lewin, E., Ito, H., Pezard, P., Ildefonse, B., 2004. Textural evidence for recent co-seismic circulation of fluids in the Nojima fault zone, Awaji island, Japan. Tectonophysics, 378, 165-181.

Brantut, N., 2020. Dilatancy-induced fluid pressure drop during dynamic rupture: Direct experimental evidence and consequences for earthquake dynamics. Earth and Planetary Science Letters, 538, 116179.

Braunagel, M.J., Griffith, W.A., 2019. The effect of dynamic stress cycling on the compressive strength of rocks. Geophysical Research Letters, 46, 6479–6486.

Brune, J.N., 2001. Fault normal dynamic loading and unloading: an explanation for "non-gouge" rock powder and lack of fault-parallel shear bands along the San Andreas fault. EOS Trans. Am. Geophys. Union, 82.

Caracausi, A., Paternoster, M., 2015. Radiogenic helium degassing and rock fracturing: A case study of the southern Apennines active tectonic region. Journal of Geophysical Research, 120, 2200-2211, doi:10.1002/2014JB011462.

Castorina, F., Masi, U., Billi, A., 2020. Assessing the origin of Sr and Nd isotopes and (REE+ Y) in Middle-Upper Pleistocene travertines from the Acquasanta Terme area (Marche, central Italy) and implications for neotectonics. Applied Geochemistry, 117, 104596.

Coppola, M., Correale, A., Barberio, M.D., Billi, A., Cavallo, A., Fondriest, M., Nazzari, M., Paonita, A., Romano, C., Stagno, V., Viti, C., Vona, A., 2021. Meso- to nano-scale evidence of fluid-assisted co-seismic slip along the normal Mt. Morrone Fault, Italy: implications for earthquake hydrogeochemical precursors. Earth and Planetary Science Letters, 568, 117010, https://doi.org/10.1016/j.epsl.2021.117010.

Cortinovis, S., Balsamo, F., Storti, F., 2019. Influence of analytical operating procedures on particle size distributions in carbonate cataclastic rocks. Journal of Structural Geology, 128,103884, https://doi.org/10.1016/j.jsg.2019.103884

Di Luccio, F., Chiodini, G., Caliro, S., Cardellini, C., Convertito, V., Pino, N.A., Tolomei, C., Ventura, G., 2018. Seismic signature of active intrusions in mountain chains. Science Advances, 4, e1701825.

Doan, M.-L., Gary, G., 2009. Rock pulverization at high strain rate near the San Andreas fault. Nature Geoscience, 2, 709–712.

Doan, M.-L., Billi, A., 2011. High strain rate damage of Carrara marble. Geophysical Research Letters, 38, L19302, https://doi.org/10.1029/2011GL049169

Doan, M.-L., D'Hour, V., 2012. Effect of initial damage on rock pulverization along faults. Journal of Structural Geology, 45, 113-124, doi:10.1016/j.jsg.2012.05.006

Dor, O., Ben-Zion, Y., Rockwell, T.K., Brune, J., 2006. Pulverized rocks in the Mojave section of the San Andreas Fault Zone. Earth and Planetary Science Letters, 245, 642–654.

Erlanger, E.D., Fellin, M.G., Willett, S.D., 2022. Exhumation and erosion of the Northern Apennines, Italy: new insights from low-temperature thermochronometers. Solid Earth, 13, 347–365, https://doi.org/10.5194/se-13-347-2022

Fondriest, M., Doan, M.L., Aben, F., Fusseis, F., Mitchell, T.M., Voorn, M., Secco, M., Di Toro, G., 2017. Static versus dynamic fracturing in shallow carbonate fault zones. Earth and Planetary Science Letters, 461, 8–19.

Galli, P.A.C., Naso, J.A., 2009. Unmasking the 1349 earthquake source (southern Italy): paleoseismological and archaeoseismological indications from the Aquae Iuliae fault. Tectonophysics, 31, 128-149, https://doi.org/10.1016/j.jsg.2008.09.007

Griffith, W.A., St. Julien, R.C., Ghaffari, H.O., Barber, T.J., 2018. A tensile origin for fault rock pulverization. Journal of Geophysical Research,123, 7055–7073.

Hesse, M., Asetre, P., Anderson, R., Edwards, C., Lee, C., Malpica, O., Klein, B., 2022. Experimental demonstration of comminution with transcritical carbon dioxide cycles. Powder Technology, 407, 117615, https://doi.org/10.1016/j.powtec.2022.117615.

Iannace, A., Capuano, M., Galluccio, L., 2011. "Dolomites and dolomites" in Mesozoic platform carbonates of the Southern Apennines: Geometric distribution, petrography and geochemistry. Palaeogeography, Palaeoclimatology, Palaeoecology, 310, 324-339.

Italiano, F., Martelli, M., Martinelli, G., & Nuccio, P. M. (2000). Geochemical evidence of melt intrusions along lithospheric faults of the Southern Apennines, Italy: geodynamic and seismogenic implications. Journal of Geophysical Research: Solid Earth, 105(B6), 13569-13578.

Kaminskaite, I., Fisher, Q.J., Michie, E.A.H., 2020. Faults in tight limestones and dolostones in San Vito lo Capo, Sicily, Italy: internal architecture and petrophysical properties. Journal of Structural Geology, 132, 103970.

Malinverno, A., Ryan, W.B., 1986. Extension in the Tyrrhenian Sea and shortening in the Apennines as result of arc migration driven by sinking of the lithosphere. Tectonics, 5, 227-245.

Melosh, B.L., Rowe, C.D., Smit, L., Groenewald, C., Lambert, C.W., Macey, P., 2014. Snap, Crackle, Pop: Dilational fault breccias record seismic slip below the brittle–plastic transition. Earth and Planetary Science Letters, 403, 432-445.

Mitchell, T.M., Ben-Zion, Y., Shimamoto, T., 2011. Pulverized fault rocks and damage asymmetry along the Arima Takatsuki Tectonic Line, Japan. Earth and Planetary Science Letters, 308, 284–297.

Mitchell, T.M., Billi, A., Miller, S.A., Goldsby, D.L., Scholz, C.H., Gran, J. K., Simons, J., 2013. Dynamic pulverization by rapid decompression. Eos Transactions AGU, Fall Meeting Supplement, Abstract MR41B–04.

Mostardini, F., Merlini, S., 1986. Appennino centro merdionale. Sezioni geologiche e proposta di modello strutturale. Memorie della Società Geologica Italiana, 35, 177-202.

Muto, J., Nakatani, T., Nishikawa, O., Nagahama, H., 2015. Fractal particle size distribution of pulverized fault rocks as a function of distance from the fault core. Geophysical Research Letters, 42, 3811–3819, https://doi.org/10.1002/2015GL064026

Orr, F.M., 2009. Onshore Geologic Storage of CO_2. Science, 325, 1656-1658.

Ostermeijer, G.A., Aben, F.M., Mitchell, T.M., Rockwell, T.K., Rempe, M., Farrington, K., 2022. Evolution of co-seismic off-fault damage towards pulverization. Earth and Planetary Science Letters, 579, 117353.

Payne, R.M., Duan, B., 2017. Insights into pulverized rock formation from dynamic rupture models of earthquakes. Geophysical Journal International, 208, 715–723, https://doi.org/10.1093/gji/ggw436.

Reches, Z., Dewers, T.A., 2005. Gouge formation by dynamic pulverization during earthquake rupture. Earth and Planetary Science Letters, 235, 361-374.

Rempe, M., Mitchell, T., Renner, J., Nippress, S., Ben-Zion, Y., Rockwell, T., 2013. Damage and seismic velocity structure of pulverized rocks near the San Andreas Fault, Journal of Geophysical Research, 118, 2813–2831.

Rockwell, T., Sisk, M., Girty, G., Dor, O., Wechsler, N., Ben-Zion, Y., 2009. Chemical and physical characteristics of pulverized Tejon Lookout granite adjacent to the San Andreas and Garlock Faults: implications for earthquake physics. Pure and Applied Geophysics, 166, 1725–1746.

Rodríguez-Escudero, E., Martínez-Díaz, J.J., Giner-Robles, J.L., Tsige, M., Cuevas-Rodríguez, J., 2020. Pulverized quartz clasts in gouge of the Alhama de Murcia fault (Spain): Evidence for coseismic clast pulverization in a matrix deformed by frictional sliding. Geology, 48, 283–287.

Rouchon, V., Gillot, P.Y., Quidelleur, X., Chiesa, S., Floris, B., 2008. Temporal evolution of the Roccamonfina volcanic complex (Pleistocene), Central Italy. Journal of Volcanology and Geothermal Research,177, 500-514.

Rowe, C.D., Griffith, W.A., 2015. Do faults preserve a record of seismic slip: A second opinion. Journal of Structural Geology, 78, Pages 1-26

Santo, A., Santangelo, N., Balassone, G., Strauss, H., 2019. Deep seated fault-related volcanogenic H_2S as the key agent of high sinkhole concentration areas. Earth Surface Processes and Landforms, 44, 713–735.

Sagy, A., Korngreen, D., 2012. Dynamic branched fractures in pulverized rocks from a deep borehole. Geology, 40, 799–802.

Schröckenfuchs, T., Bauer, H., Grasemann, B., Decker, K., 2015. Rock pulverization and localization of a strike-slip fault zone in dolomite rocks (Salzach–Ennstal–Mariazell–Puchberg fault, Austria). Journal of Structural Geology, 78, 67–85.

Sibson, R.H., 1987. Earthquake rupturing as a mineralizing agent in hydrothermal systems. Geology, 15, 701-704.

Smeraglia, L., Berra, F., Billi, A., Boschi, C., Carminati, E., Doglioni, C., 2016. Origin and role of fluids involved in the seismic cycle of extensional faults in carbonate rocks. Earth and Planetary Science Letters, 450, 292-305.

Smeraglia, L., Bernasconi, S.M., Berra, F., Billi, A., Boschi, C., Caracausi, A., Carminati, E., Castorina, F., Doglioni, C., Italiano, F., Rizzo, A.L., Uysal, T., Zhao, J.-x., 2018. Crustal-scale fluid circulation and co-seismic shallow comb-veining along the longest normal fault of the central Apennines, Italy. Earth and Planetary Science Letters, 498, 152-168.

Smith, Z.D., Griffith, W.A., 2022a. Evolution of pulverized fault zone rocks by dynamic tensile loading during successive earthquakes. Geophysical Research Letters, https://doi.org/10.1029/2022GL099971

Smith, Z.D., Griffith, W.A., 2022b. Lithological controls on fault damage zone development by coseismic tensile loading. Tectonophysics, 838, 229471, https://doi.org/10.1016/j.tecto.2022.229471.

Tarasewicz, J.P.T., Woodcock, N.H., Dickson, J.A.D., 2005. Carbonate dilation breccias: examples from the damage zone to the Dent Fault, northwest England. Geological Society of America Bulletin, 117, 736-745.

van der Meer, L.G.H., Hofstee, C., Orlic, B., 2009. The fluid flow consequences of CO_2 migration from 1000 to 600 metres upon passing the critical conditions of CO_2. Energy Procedia, 1, 3213–3220.

Yuan, F., Prakash, V., Tullis, T., 2011. Origin of pulverized rocks during earthquake fault rupture. Journal of Geophysical Research, 116, B06309, doi: 10.1029/2010JB007721.

Wechsler, N., Allen, E.E., Rockwell, T.K., Girty, G., Chester, J.S., Ben-Zion, Y., 2011. Characterization of pulverized granitoids in a shallow core along the San Andreas Fault, Littlerock, CA, Geophysical Journal International, 186, 401–417.

Williams, R.T., Rowe, C.D., Okamoto, K., Savage, H.M., Eves, E., 2021. How fault rocks form and evolve in the shallow San Andreas fault. Geochemistry, Geophysics, Geosystems, 22, e2021GC010092, https://doi.org/10.1029/2021GC010092

Wilson, B., Dewers, T., Reches, Z., Brune, J., 2005. Particle size and energetics of gouge from earthquake rupture zones. Nature, 434, 749–752.

Xu, S., Ben-Zion, Y., 2017. Theoretical constraints on dynamic pulverization of fault zone rocks. Geophysical Journal International, 209, 282–296, https://doi.org/10.1093/gji/ggx033.

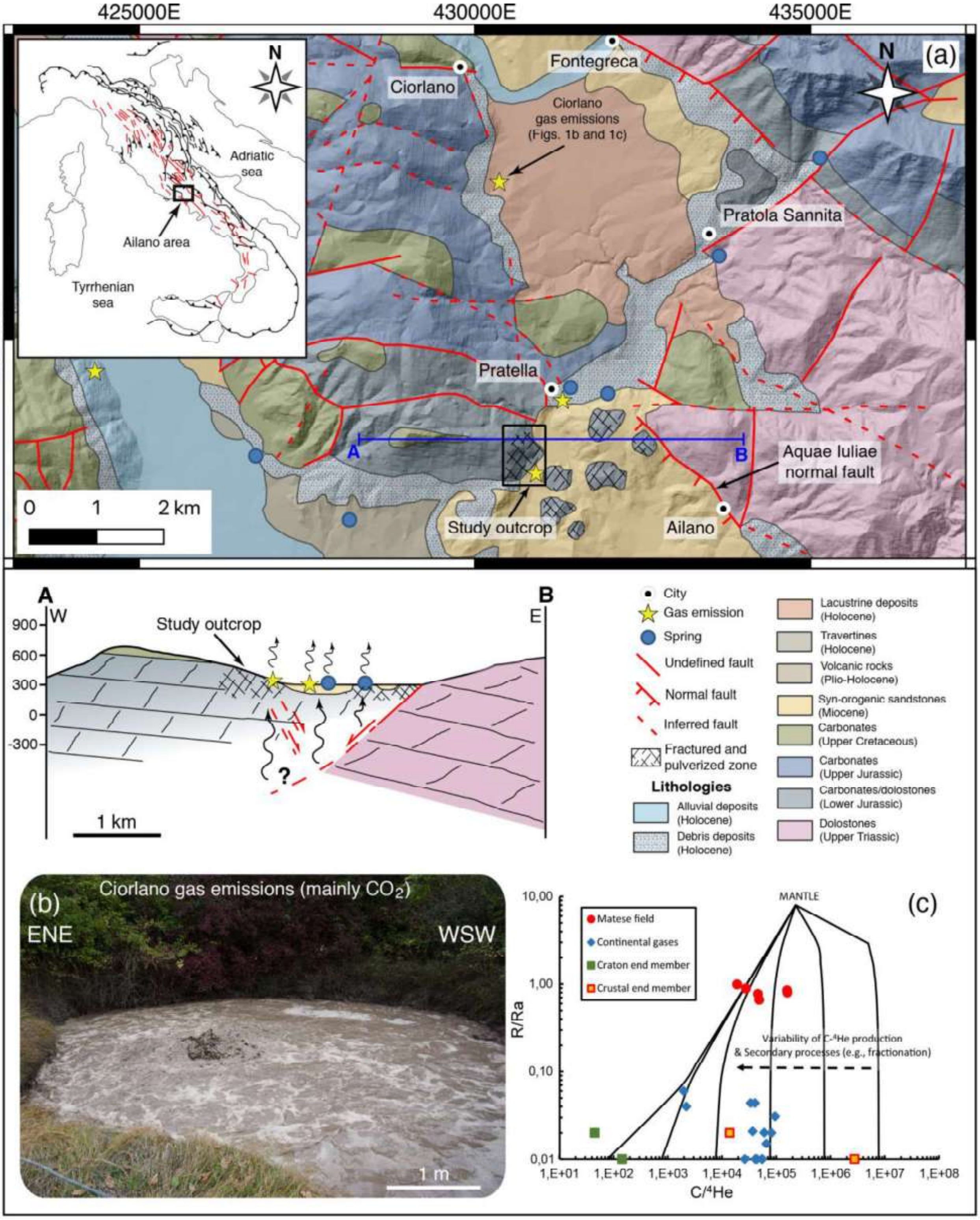

Figure 1. Geological setting. **(a)** Geological setting of the study area. Inset shows location of the study area in Italy, wherein red faults are main active normal faults and black faults are main thrusts. See, below the map, a geological cross-section through the study area, showing that the studied exposure is located at the hanging wall of a normal fault system

with active CO_2-rich springs and vents. **(b)** Photograph of the Ciorlano active CO_2-rich spring nearby the studied rock exposure (see the map for its location). **(c)** Geochemical data from the Ciorlano spring and nearby springs (see the Hydrothermal Setting section for further information). Data plotted in this diagram are in Table S1.

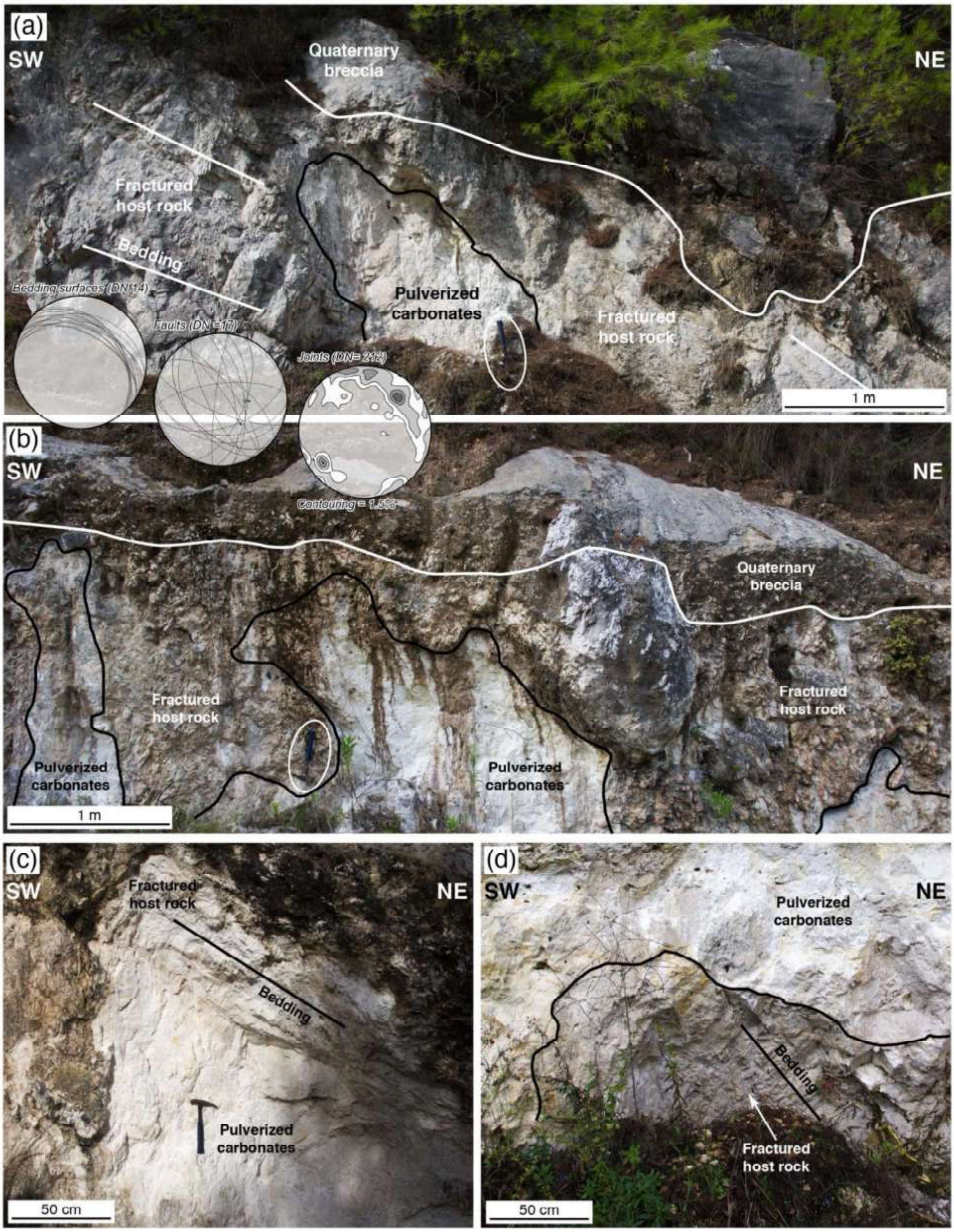

Figure 2. Exposure scale photographs (see also Videos S1-S4 and Virtual Outcrops S1-S4). **(a, b)** Panoramic views of the pulverized dolostones showing domal and chimney-like structures (pulverized pockets in the text) within bedded dolostone. Note the unconformity between the carbonates and the overlying Quaternary slope debris deposits. Three Schmidt

polar plots (lower hemisphere; Table S3) in (a) show, from left to right, attitudes of bedding surfaces, normal faults, and joints (represented as contours to joint poles), respectively, measured along the studied exposure. **(c, d)** Pockets of pulverized dolostones where primary structures such as bedding are still preserved although finely pulverized.

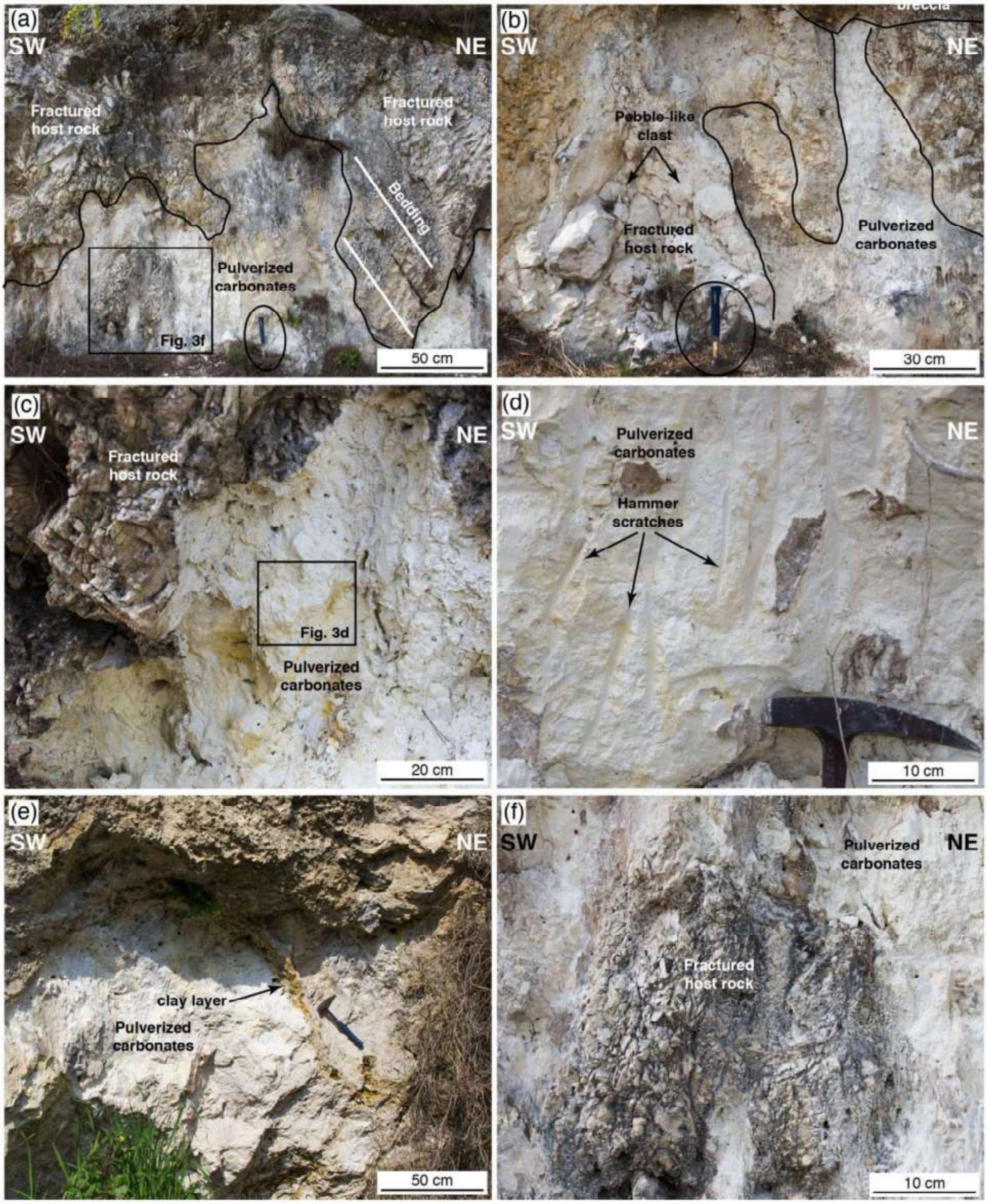

Figure 3. Exposure scale photographs (see also Videos S1-S4 and Virtual Outcrops S1-S4). **(a)** Pockets of pulverized dolostones embedded within highly fractured dolostone beds. **(b)** Pulverized dolostones with preserved pebble-like clasts of host rock. **(c)** Boundary between the pulverized dolostones and the fractured host rock. **(d)** Detail of pulverized

dolostones showing scratches created by the hammer to test the physical status of the rock. **(e)** Antiformal clay-rich layer at the top of a pocket of pulverized dolostones. **(f)** Lens of highly fractured host rock preserved within pulverized dolostones.

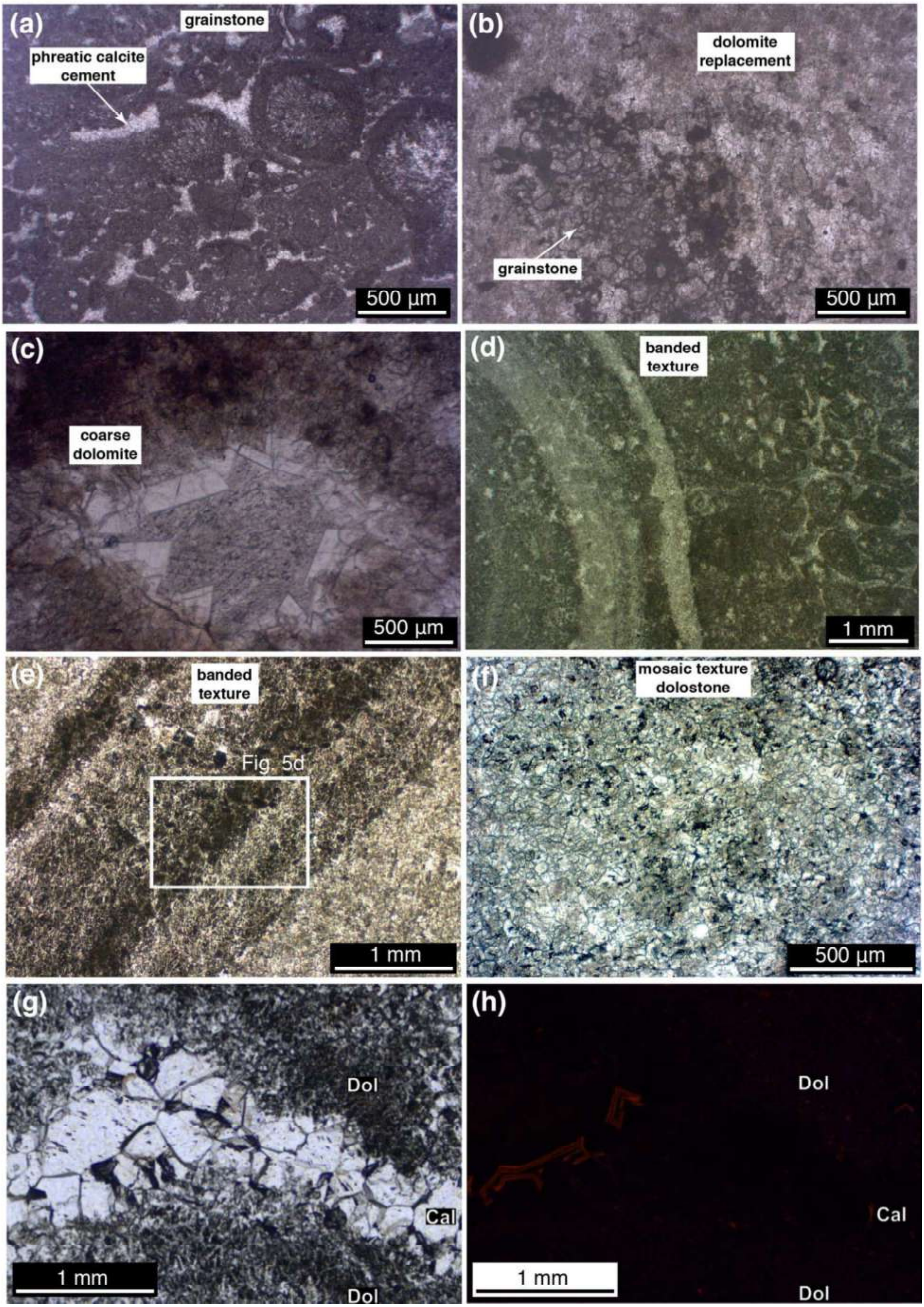
(a)
grainstone
phreatic calcite cement
500 µm
(b)
dolomite replacement
grainstone
500 µm
(c)
coarse dolomite
500 µm
(d)
banded texture
1 mm
(e)
banded texture
Fig. 5d
1 mm
(f)
mosaic texture dolostone
500 µm
(g)
Dol
Cal
1 mm
Dol
(h)
Dol
Cal
1 mm
Dol

760

Figure 4. Microscopic photographs (see also Figs. S1-S4). **(a,b)** Distal carbonate host rock showing primary depositional features and evidence of diagenetic dolomitization. **(c)** Coarse secondary dolomite filling a void within distal carbonate host rock. **(d)** Proximal fractured host rock collected close to the pulverized dolostones, showing a banded texture. **(e)** Detail of banded texture showing fine-grained dolomite crystals. **(f)** Mosaic or crackle-like texture within the fine-grained dolomite crystals. **(g,h)** Calcite crystals filling a fracture and showing a dull red zoned luminescence color.

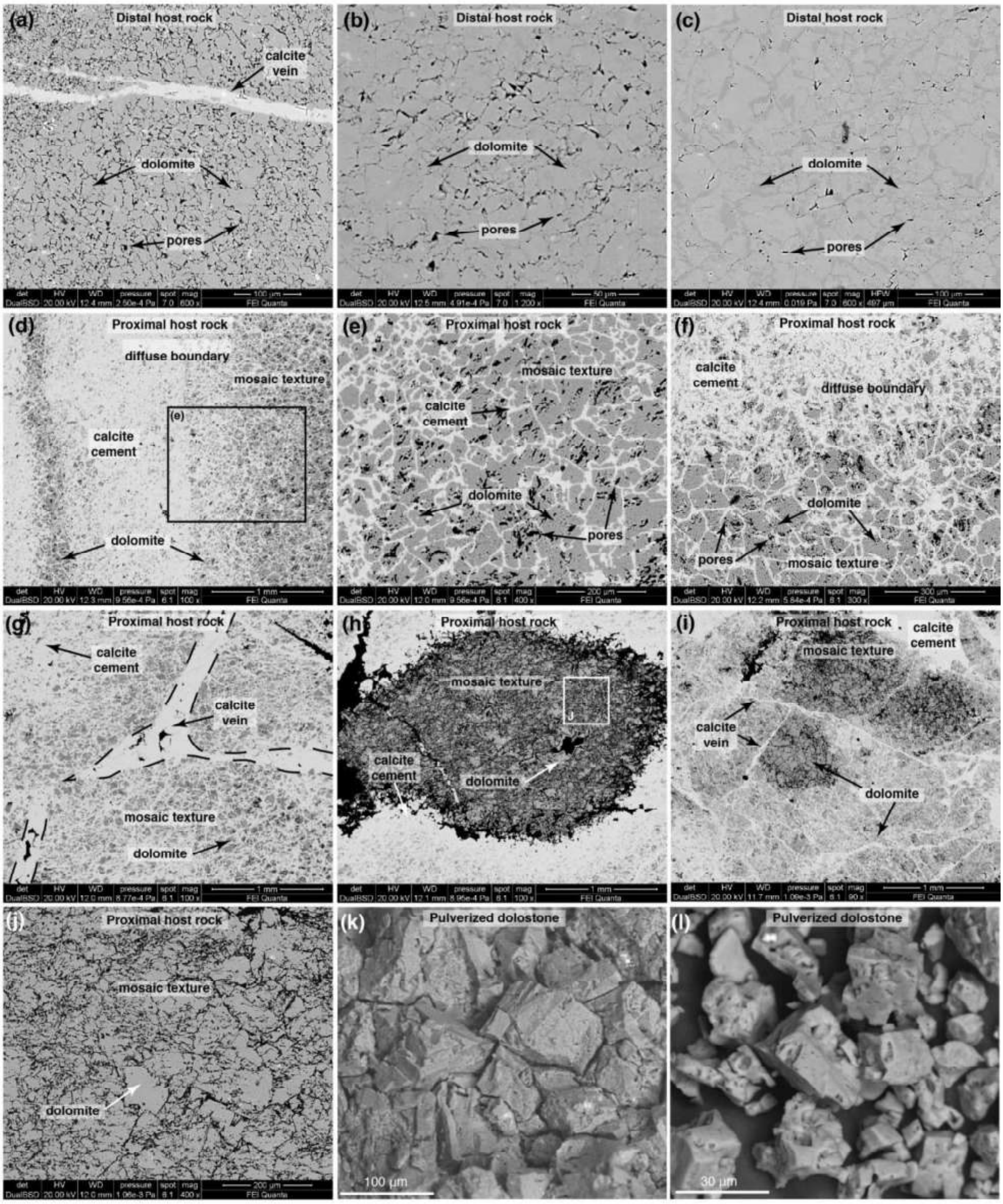

Figure 5. Microscopic photographs (see also Figs. S1-S4). **(a-c)** Microscale texture of the distal carbonate host rock showing fine-grained dolomite crystals cut, in (a), by a calcite filled vein. **(d)** Proximal host rock showing a banded texture with alternating bands made of fine dolomite grains cemented by microcrystalline calcite. **(e,f)** Details of the fine dolomite grains

showing a mosaic or crackle-like texture with sharp grain boundaries (e) and a diffuse boundary between the dolomite grains and the microcrystalline calcite (f). **(g)** Calcite filled vein cutting the banded texture. **(h,i)** Proximal host rock showing lenses of fine dolomite grains with a crackle-like texture, sharp grain boundaries, and lack of microcrystalline calcite between the crystals. Compare these microphotographs with figure S2d in Coppola et al., (2021). **(j)** Detail of fine dolomite grains showing a crackle-like (or masaic) texture and lack of microcrystalline calcite between the grains. **(k,l)** Details of the pulverized and incohesive dolostones characterized by fine dolomite grains with rhomboidal shapes and sharp boundaries.

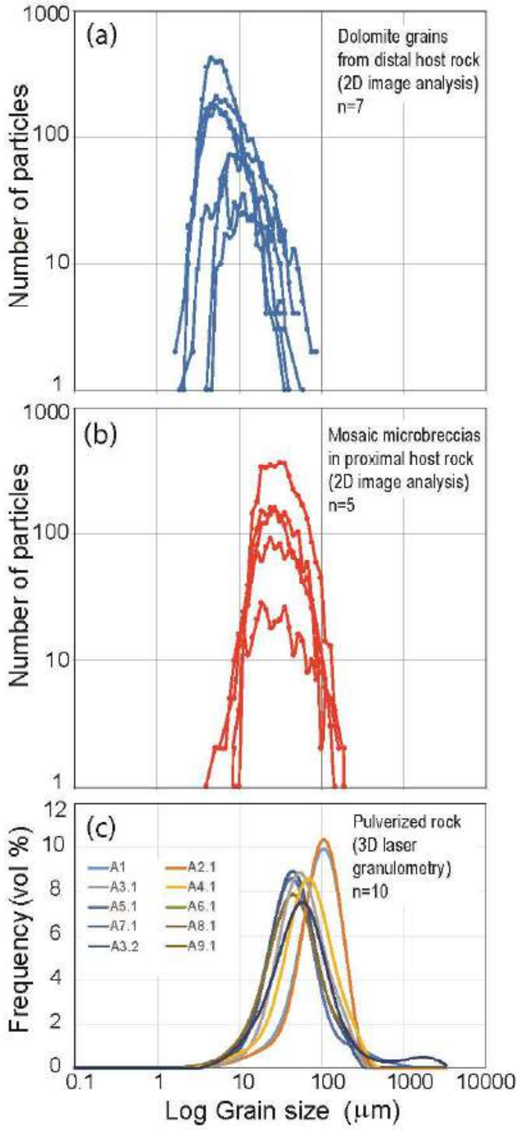

(a)
Dolomite grains from distal host rock (2D image analysis) n=7
Number of particles
1000
100
10
1
(b)
Mosaic microbreccias in proximal host rock (2D image analysis) n=5
Number of particles
1000
100
10
1
(c)
Pulverized rock (3D laser granulometry) n=10
Frequency (vol %)
12
10
8
6
4
2
0
A1
A2.1
A3.1
A4.1
A5.1
A6.1
A7.1
A8.1
A3.2
A9.1
0.1
1
10
100
1000
10000
Log Grain size (μm)

Figure 6. Grain size distributions (see also Figs. S5-S18 and Tables S4-S5). **(a)** Dolomite grains (i.e. crystals) from distal host rock (2D analysis). **(b)** Dolostone grains (mostly crystal aggregates, more rarely single crystals) from cemented crackle breccias in the proximal host rock (2D analysis). **(c)** Dolostone grains (mostly crystal aggregates, more rarely single crystals) from incohesive pulverized pockets of rocks (3D analysis).

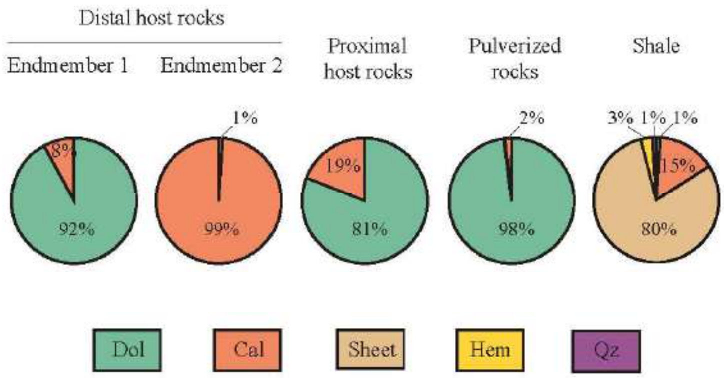

Distal host rocks
Endmember 1
Endmember 2
Proximal host rocks
Pulverized rocks
Shale
8%
92%
1%
99%
19%
81%
2%
98%
3%
1%
1%
15%
80%
Dol
Cal
Sheet
Hem
Qz

Figure 7. X-ray semiquantitative analysis of distal (e.g. Figs. 4a-4c) and proximal (e.g. Figs. 5d-5i) carbonate host rocks, pulverized rocks (e.g. Figs. 5k and 5l), and shales (or clay-rich layers; e.g. Fig. 3e) interbedded with dolostone layers (Table S6). Dol-dolomite, Cal-calcite, Sheet-Sheet silicate, Hem-hematite, Qz-quartz. Numbers refer to average values.

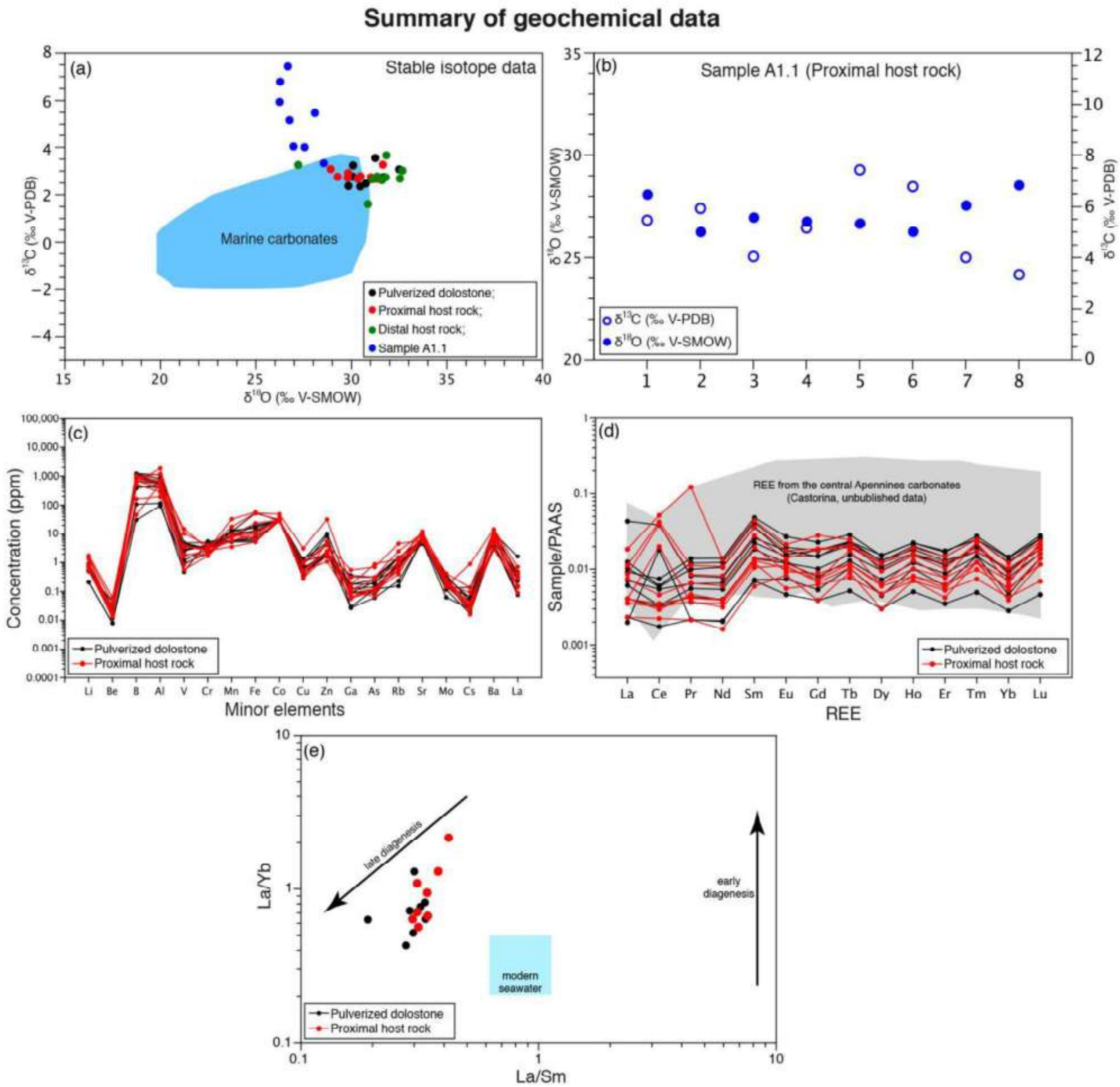

Figure 8. Geochemical data (Tables S7 and S8). **(a)** Diagram showing $\delta^{13}C$ vs. $\delta^{18}O$ values. Note that pulverized carbonates have the same $\delta^{13}C$ and $\delta^{18}O$ values of those from distal

and proximal host rocks (bulk analyses). Micro-subsamples (punctual analysis) of calcite precipitates from sample A1.1 (Fig. S19; proximal host rock) show a large variability of $\delta^{13}C$ values and $\delta^{18}O$ values lower than those of all other samples. **(b)** Diagram showing $\delta^{13}C$ and $\delta^{18}O$ values vs. the sampling distance along the microscale transect (sample A1.1; Fig. S19). **(d)** Diagram for the concentration of minor elements. **(e)** REE concentration vs. Sample/PAAS showing that all the analyzed samples (pulverized carbonates and host rocks) are in the range of REE value or marine carbonates of the central Apennines (bulk chemical analysis). **(f)** La/Sm vs. La/Yb diagram showing that all samples have a late diagenetic imprint (bulk chemical analysis).

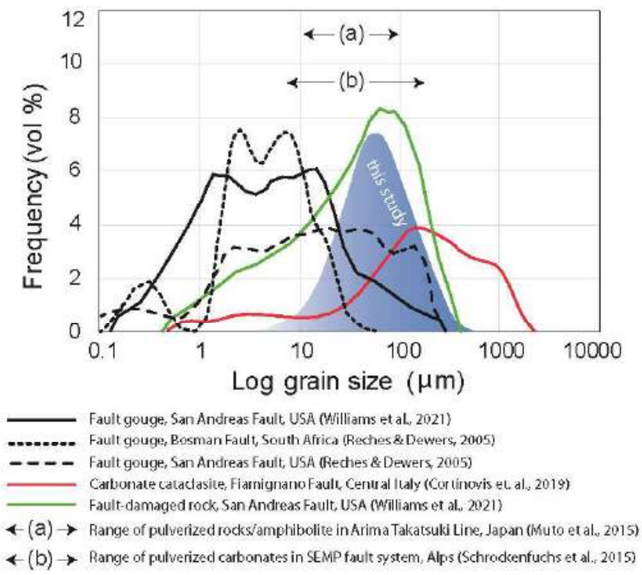

12
10
8
6
4
2
0
Frequency (vol %)
0.1
1
10
100
1000
10000
Log grain size (μm)
(a)
(b)
this study
Fault gouge, San Andreas Fault, USA (Williams et al., 2021)
Fault gouge, Bosman Fault, South Africa (Reches & Dewers, 2005)
Fault gouge, San Andreas Fault, USA (Reches & Dewers, 2005)
Carbonate cataclasite, Fiamignano Fault, Central Italy (Cortinovis et. al., 2019)
Fault-damaged rock, San Andreas Fault, USA (Williams et al., 2021)
(a) Range of pulverized rocks/amphibolite in Arima Takatsuki Line, Japan (Muto et al., 2015)
(b) Range of pulverized carbonates in SEMP fault system, Alps (Schrockenfuchs et al., 2015)

Figure 9. Comparison of grain size distributions between the pulverized rocks studied in this work (average curve in blue) and other fault-related pulverized rocks from the San Andreas Fault in California (Reches and Dewers, 2005; Williams et al., 2021), the Salzach-Ennstal-Mariazell-Puchberg (SEMP) fault system in the Northern Calcareous Alps, Austria (Schrockenfuchs et al., 2015), the Bosman Fault in South Africa (Reches and Dewers, 2005), and the Arima Takatsuki Line in Japan (Muto et al., 2015). For comparison, the grain size distribution curves of carbonate cataclasites and gouges from tectonically active localities in Italy (Cortinovis et al., 2021) are also plotted. Compared to fault-related cataclasites and gouges, the pulverized rocks have narrower grain size ranges and symmetrical, unimodal distributions.

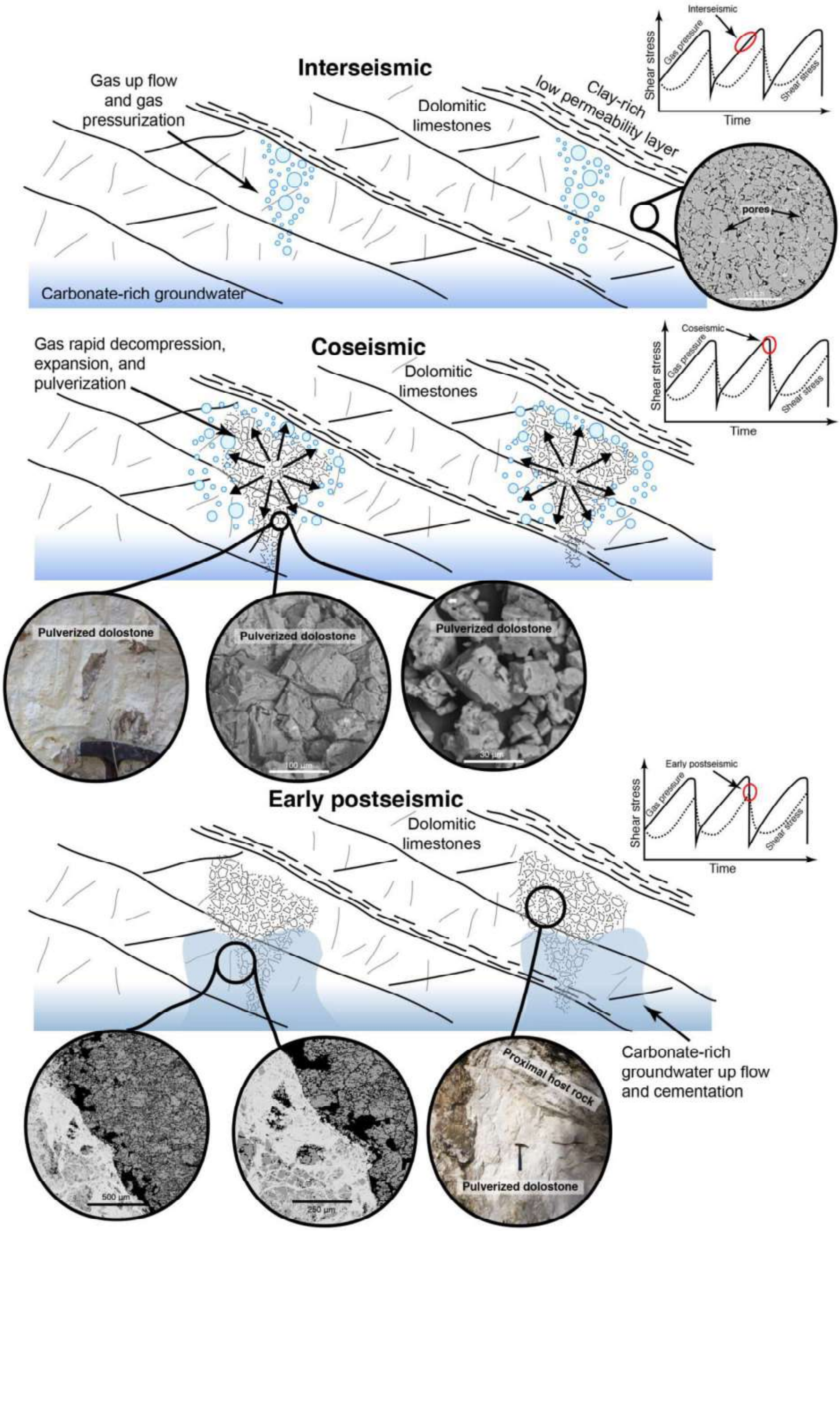
Interseismic
Gas up flow
and gas
pressurization
Dolomitic
limestones
Clay-rich
low permeability layer
pores
Carbonate-rich groundwater
Interseismic
Shear stress
Gas pressure
Shear stress
Time
Coseismic
Gas rapid decompression,
expansion, and
pulverization
Dolomitic
limestones
Coseismic
Pulverized dolostone
Pulverized dolostone
Pulverized dolostone
100 μm
30 μm
Early postseismic
Dolomitic
limestones
Early postseismic
Carbonate-rich
groundwater up flow
and cementation
Proximal host rock
Pulverized dolostone
500 μm
250 μm

Figure 10. Synthetic model of dolostone pulverization. During inter- to pre-seismic stages, CO_2-rich gases accumulate and become pressurized in pockets of microporous dolostones at the top of a bicarbonate-rich aquifer. Likely during coseismic stages, the rock volume is rapidly decompressed and, where the permeability is sufficiently low to prevent a rapid escape of the gas from the rock, the trapped gas itself rapidly expand within the dolomitic rock, pulverizing it in situ. Soon after this stage, the decompression as well as the new porosity generated by the pulverization attracts the bicarbonate-rich waters, which rapidly degas (CO_2) and precipitate a microcrystalline calcite cement that fossilizes the newly pulverized rock forming a cemented micro-mosaic or micro-crackle breccia. The cementation is so rapid that forms a sort of impermeable halo around the pocket of incoherent pulverized dolostone, preventing its cementation.